CrossMark

Chromospheric Carbon Monoxide Formation around a Solar Pore

Johnathan R. Stauffer[1] (ID), Kevin P. Reardon[1,2] (ID), and Matt Penn[3]

[1] Department of Astrophysical and Planetary Sciences, 391 UCB, 2000 Colorado Ave, Boulder, CO 80309, USA
[2] National Solar Observatory, 3665 Discovery Dr, Boulder, CO 80303, USA
[3] Raytheon Technologies, 1151 E Hermans Rd, Tucson, AZ 85756, USA

Abstract

We present observations of NOAA AR 11159, obtained on 2011 February 14 in the 4.7 μm band of carbon monoxide (CO) and coordinated with spectroscopic imaging of three atomic lines (Na I 5896 Å, Fe I 7090 Å, and Ca II 8542 Å) which sample heights from the mid-photosphere to the chromosphere. Phase-difference spectra between the observed spectral lines instead indicate that the CO lines form at $z \approx 530-650$ km in the quiet Sun. During the two hours of observations, seven long-lived cooling events ("cold bubbles") were observed in CO in the region surrounding a large pore, but were not visible in the three atomic lines. These events show self-similar temporal evolution with time scales consistent with the chemical formation rate of CO at $z \approx 1000$ km. Due to the lack of such features in the surrounding quiet Sun, we hypothesize that the magnetic canopy field surrounding the pore, which suppresses the upward propagation of acoustic waves into the chromosphere and the subsequent formation of shocks, depresses the rate of acoustic heating and allows CO to condense and cool the atmosphere at those heights. These "cold bubbles" may be a source of the chromospheric CO that produces the unexpectedly high ($z \approx 1000$ km) limb extensions seen in the stronger CO lines, and may provide a unique opportunity to study this enigmatic component of the solar atmosphere in spatially resolved observations.

1. Introduction

Traditional semiempirical models of the solar atmosphere (e.g., Fontenla et al. 1993) present a well-ordered view of the Sun, with a smooth decline in temperature from the solar interior to a ~ 4400 K *temperature minimum* at $z \approx 500$ km above the solar surface, then rising in the *chromosphere* where it plateaus at $T \approx 6000$–10,000 K. The chromosphere is, in turn, bounded from above by the *transition region* at $z \approx 2000$ km, marking the base of the solar *corona*. While these hydrostatic models are clearly a simplification of the real Sun, they are capable of reproducing a wide variety of spectral lines from the infrared (IR) to the ultraviolet. Because of this predictive capacity, they are often used to contextualize solar observations, which are often limited to a small number of spectral diagnostics. This is particularly important in studies of the chromosphere, since the few lines opaque enough to be sensitive to that region are often dominated by the effects of non-local thermodynamic equilibrium (NLTE) radiative transfer, complicating their interpretation.

However, certain features of the solar spectrum shed doubt on this model of a ubiquitously hot chromosphere. Early measurements of the fundamental ($\Delta \nu = 1$) molecular band of carbon monoxide (CO) by Noyes & Hall (1972) showed unexpectedly cool ($T \approx 3500$ K) line core temperatures at the extreme Solar limb, which were then attributed to emission from cool granular downflow lanes. However, in later observations, Ayres & Testerman (1981) found that the center-to-limb behavior of the temperatures inferred from these

lines, which they found to range from ~ 4000 K near disk center to as low as 3700 K at the extreme limb, were better explained by the elimination of the traditional chromospheric temperature rise at $z \approx 500$ km. This conclusion was bolstered by measurements of the extent of limb emission from CO, which showed significant amounts of CO at as far as 1000 km above the solar surface (Solanki et al. 1994). Combined, these observations suggest that cool, sub-4000 K gas is present beyond the canonical heights of the "temperature minimum" and into the lower layers of the chromosphere, which should be too hot to sustain significant amounts of CO according to traditional models.

Early attempts to model the formation of chromospheric CO posited a static "COmosphere" (e.g., Avrett 1995; Ayres & Rabin 1996; Ayres 2003; Ayres et al. 2006), predicting that the low chromosphere (described by classical "hot" models) is permeated by cool, CO-rich "clouds." These were described by an additional "cold" 1D atmospheric model featuring an extended temperature minimum, tuned to reproduce the CO line core intensities and limb extensions. Such approaches yield a two-peaked contribution function for many of the CO spectral lines, indicating that their intensities are determined both by the conditions in the upper photosphere and the chromosphere. At disk center, this contribution is approximately equal, while near the limb it shifts to depend primarily on the chromospheric temperature due to the increased opacity along the inclined line of sight. While such two-component models are capable of reproducing the average spectrum and limb extension of solar CO, spatially resolved observations of these lines do not reveal any visible bifurcation of the chromosphere. To remain undetected by a 1.6 m telescope such as the McMath-Pierce Solar Telescope, the cold regions of the atmosphere must exist only at spatial scales less than 0$\farcs$4 (Ayres 2003), smaller than

the scale of the solar granulation. The existence of such small features is unlikely, as they would quickly equilibrate with the hotter surrounding atmosphere through turbulent mixing.

Alternatively, high-altitude CO can be interpreted as a byproduct of chromospheric dynamics. For example, CO can form in the cooling, rarefacted wake of large amplitude acoustic waves propagating in the chromosphere. Early 1D models proposed by Carlsson & Stein (1995, 1997) indicated a part-time COmosphere, where the chromospheric temperature varies dramatically with the passage of these waves and shocks but its cold average temperature allows for the reproduction of the observed CO line core temperatures and limb extensions. More recent 2D modeling of the chromosphere using Bifrost (Gudiksen et al. 2011) similarly shows cool pockets forming in the wake of chromospheric shocks, which often extend as high as $z \approx 2000$ km above the solar surface (Leenaarts et al. 2011). These models indicate that the chromosphere is capable of cooling enough to form significant amounts of CO, at least in principle. However, similar models performed using CO5BOLD (Freytag et al. 2010) that incorporate time-dependent atmospheric chemistry indicate that the frequent passage of shocks in the quiet Sun prevents the accumulation of chromospheric CO (Wedemeyer-Böhm et al. 2006; Wedemeyer-Böhm & Steffen 2007), since the molecular formation is limited by long chemical reaction rates at chromospheric heights (Ayres & Rabin 1996).

New observations are sorely needed to understand the nature of solar CO and the formation of its spectral lines. While the development of new instruments with increased spatial and spectral resolution is imperative to distinguish between these competing models (Ayres 2003), it is likely that better observation of these lines alone will not be enough to resolve the controversies surrounding solar CO. Instead, we will need to rely on multi-wavelength observations to provide additional context to the CO lines in order to resolve the mysteries surrounding their formation. By choosing an ensemble of spectral lines with complementary regions of sensitivity, one can construct a more complete view of the behavior of the solar atmosphere beyond what any single line can provide. This additional context is especially important when studying lines with uncertain or ambiguous line formation characteristics, such as the CO fundamental band, by carefully selecting complementary spectral diagnostics with overlapping regions of sensitivity, the ambiguity surrounding those lines' formation can be reduced. This paper marks one of the first such studies, combining wide-field observations of the CO fundamental band with high-resolution imaging spectrograph data of several atomic lines.

2. Observations

In this paper, we present observations of NOAA Active Region 11159 coordinated between the Dunn Solar Telescope (DST) and McMath-Pierce Solar Telescope (McMP) on 2011 February 14. At the DST, the Interferometric BIdimensional Spectropolarimeter (IBIS, Cavallini 2006; Reardon & Cavallini 2008) and Facility InfraRed Spectrometer (FIRS; Jaeggli et al. 2010) were used to observe the target region (but herein, we use only the IBIS data). At the McMP, the NSO Array Camera (NAC, Ayres et al. 2008) was used with the IR spectrograph to observe the same region in the mid-IR. Context images in the white light continuum, along with Dopplergrams and photospheric magnetograms were provided by the
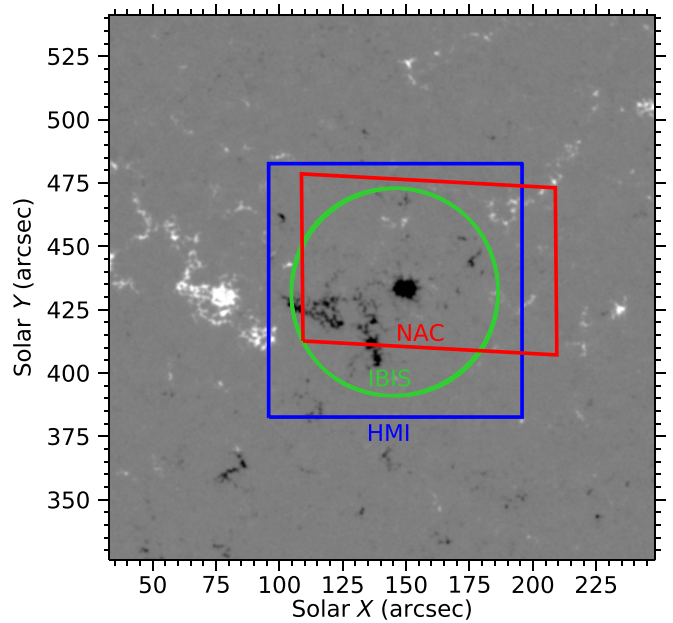
Figure 1. The approximate locations of the three instruments' fields of view, superimposed on the HMI magnetogram. The green circle represents the $\sim 80''$ aperture of IBIS (masked down from the originally observed $\sim 95''$ diameter due to image motion that caused discontinuous spatial coverage at the edge of the field stop), while the red rectangle shows the region covered by the McMP/NAC scan (the slit is oriented north/south and scans from east to west). For reference and coalignment, a $100''$ cutout from SDO/HMI (blue square) was extracted to cover the full IBIS FOV and its region of overlap with McMP/NAC.

Helioseismic and Magnetic Imager onboard the Solar Dynamics Observatory (SDO/HMI, Scherrer et al. 2011; Pesnell et al. 2012).

Figure 1 shows the HMI magnetogram of AR 11159 at the time of observation, as well as the effective fields of view of the IBIS (green) and NAC (red) instruments. Additionally, a $100''$ square HMI cutout (used as a stable spatial reference) is marked in blue. The observations are roughly centered on a large magnetic pore, which served as the AO lock point for the IBIS and McMP observations. The pore was located 9° west and 20° north of disk center at the time of our observations ($\mu = 0.91$, or $\theta = 22°$).

2.1. McMP Observations

NAC observed AR 11159 from 17:08:47 UT to 19:03:50 UT in the 4.7 μm molecular band of CO. The $0\rlap{.}''25$ wide slit spanned $55''$ in the north-south direction with a sampling of $0\rlap{.}''064$ px^{-1}, and was scanned across the region from east to west with an approximately $1''$ step size. To match this spatial under-sampling in the scan direction (and to better match the seeing-limited resolution), we binned the NAC spectra by 16 pixels along the slit, decreasing the relative noise of the CO spectrum by a factor of four and yielding an $\sim 1''$ sampling. Each slit pointing required a total integration time of 0.5 s, and a full 112-step scan was completed with a cadence of ~ 58 s.

We applied dark and flat corrections to the NAC spectra, and corrected them for rotation with respect to the detector axes and time-dependent shifts in the dispersion direction. The flat field collected by the telescope operators was constructed by fixing the telescope onto a region of quiet Sun and scanning through the IR spectrum. This has the benefit of removing spectral features from the flat field, but results in an imperfect correction

2
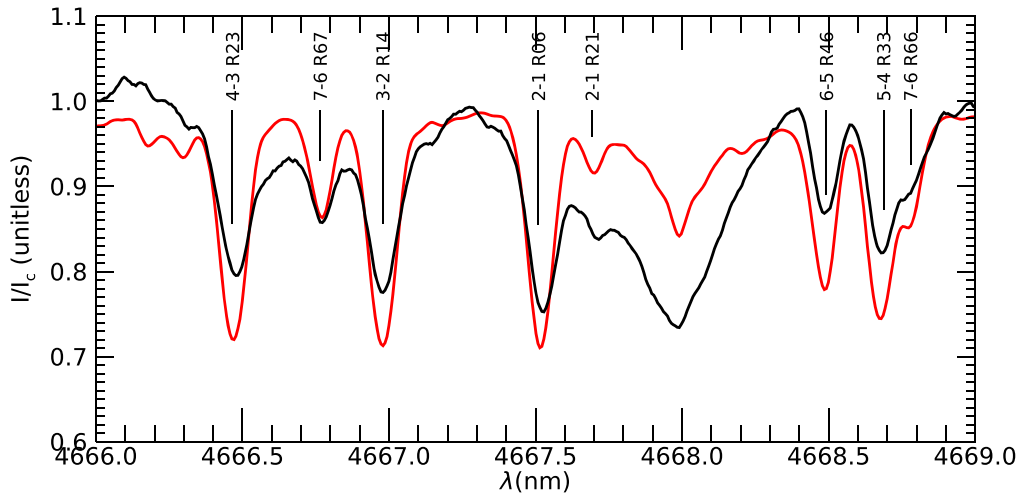
Figure 2. The quiet Sun average CO spectrum observed by McMP/NAC (black), with notable lines annotated (some weaker lines have been omitted, as they are not reliably detectable in the NAC spectra). The broad spectral feature at 4668 nm is a telluric line. For reference, the Kitt Peak IR atlas (Livingston & Wallace 1991) is shown in red, degraded to the spectral resolution of the McMP spectrograph. The feature at 4668 nm is a telluric absorption. For both spectra, the intensity has been normalized to the local average continuum intensity. Note that, even after reduction, there are still deviations in the continuum intensity of $\sim$10% (e.g., around the 7-6 R67 line). When analyzing a single line (or set of closely spaced lines), these deviations are corrected through the use of a low-order polynomial background correction.

due to the flat field being collected over a different wavelength range than the observed spectra. To correct for this, a second-order "spatial flat" was constructed by removing the average solar spectrum from the average quiet Sun spectrum observed near the western edge of the scan. A similar correction was made to account for slight shifts in the flat field over the course of the observing run.

The portion of the CO spectrum captured by NAC, averaged over a region of quiet Sun, is pictured in Figure 2. At least eight CO lines can be seen in the spectral window, including five strong lines (4-3 R23, 3-2 R14, 2-1 R06, 6-5 R46, and 5-4 R33) and three weak lines (7-6 R67, 2-1 R21, and 7-6 R66). In this paper, we focus on the behavior of the strong lines, which form higher in the atmosphere (e.g., Uitenbroek 2000) and are therefore more likely to show signatures of chromospheric CO than the weak lines. Of these, we choose 3-2 R14 as the main line of interest, as its behavior and formation has been extensively studied (e.g., Solanki et al. 1994; Uitenbroek et al. 1994; Uitenbroek 2000), and because it is well separated from other strong CO lines and the broad telluric line at 4668 nm; unless otherwise specified, "the CO line" refers to this transition.

2.2. DST/IBIS Observations

IBIS observed AR 11159 in two observing sequences: first from 17:11:14 UT to 17:15:43 UT (consisting of 13 spectral scans), and then from 17:23:17 UT to 19:01:07 UT (281 scans). Due to unstable seeing in the first observing sequence and at the end of the second sequence, we use only the first 236 scans of the second observing run, spanning from 17:23:17 UT to 18:45:15 UT (approximately 80 minutes of continuous observations).

As an imaging spectrometer, IBIS produces spatially resolved, nearly monochromatic images of the solar surface by passing the telescope beam through a pair of Fabry–Perot etalons (Cavallini 2006). By tuning the separation of the interferometer plates, the transmission profile of IBIS can be stepped across a spectral line, capturing a sequence of images that can be combined to produce a spectrum at each pixel on

the detector. For these observations, the instrument sequentially captured scans of Na I 5896 Å (D1; 31 wavelength points), Fe I 7090 Å (20 wavelength points), and Ca II 8542 Å (31 wavelength points) in spectroscopic mode (i.e., without polarimetry). Each scan step took a total integration time of $\sim$0.2 s. Accounting for a $\sim$1.4 s delay to change between prefilters for the different lines, the set of three spectral lines was observed with a cadence of $\sim$21 s. Each narrowband image was accompanied by a simultaneous broadband white light image taken through a 100 Å FWHM filter centered at 6610 Å. IBIS observed the Sun through a $\sim$90″ diameter circular field stop. In our analysis, we limited ourselves to a $\sim$80″ diameter region of interest (shown in Figure 1) to avoid data gaps, as solar features near the edge of the field stop occasionally moved out of the observed area due to atmosphere-induced motions of the image.

We applied dark, flat-field, instrumental blueshift, and fringe-removal corrections to the IBIS data, which were then interpolated onto a uniformly spaced wavelength grid. Additionally, seeing-induced distortions were removed by "destretching" the white light images such that they aligned with the closest-in-time HMI continuum image, which provides a stable reference of the solar granulation. The seeing-induced distortions were then applied to the cotemporal narrowband images and all the images mapped to a uniform, cospatial sampling of 0″1/px. Last, corrections for scattered-light contamination and attenuation by the spectral pre-filter were performed by comparing the average quiet Sun spectra to the NSO Fourier Transform Spectrometer (FTS) atlas (Kurucz et al. 1984). This calibration also provides an absolute wavelength scale for each of the scanned lines, as well as a relative intensity scale. After these corrections, the IBIS spectra are normalized to the FTS atlas continuum intensity.

The reduced spectral profiles obtained from these scans, averaged over a region of quiet Sun, are shown in Figure 3 (black) in comparison to the NSO FTS atlas (red). The diamonds represent the observed wavelength points, while the solid line shows a cubic spline interpolation of the spectrum onto a uniform wavelength grid.
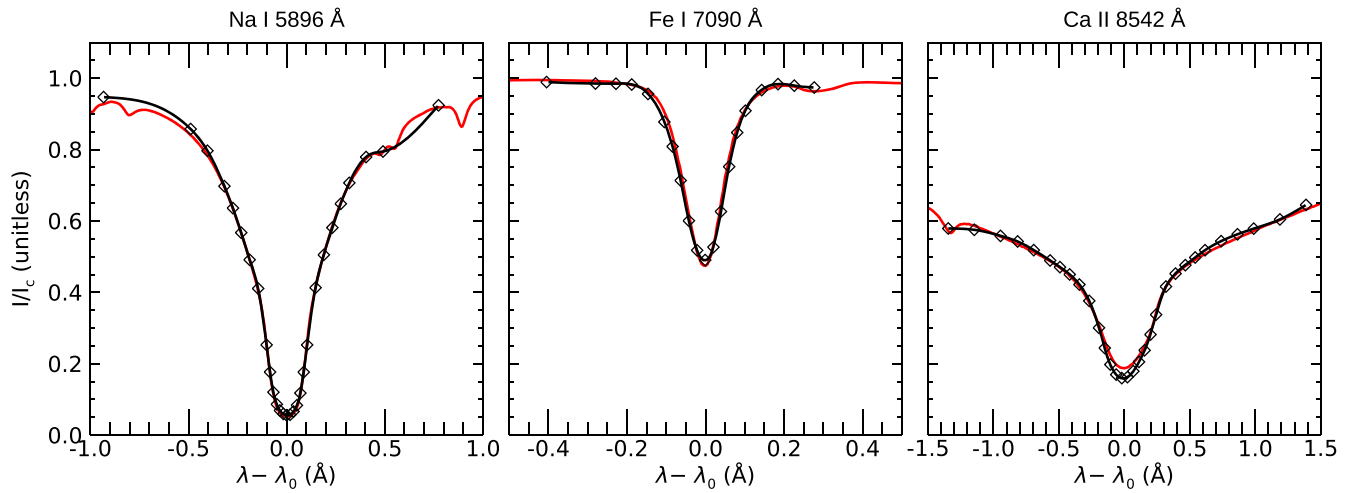
Figure 3. The quiet Sun average spectra observed by DST/IBIS (black). The wavelength positions sampled by IBIS are indicated by the black diamonds, while the solid line represents a cubic spline interpolation of the observed intensities onto an even wavelength grid. For reference, the NSO FTS atlas (Kurucz et al. 1984) is shown in red. For all spectra, the intensity has been normalized to the atlas continuum intensity, and the wavelength scale is shown relative to the rest wavelength of the line shown.
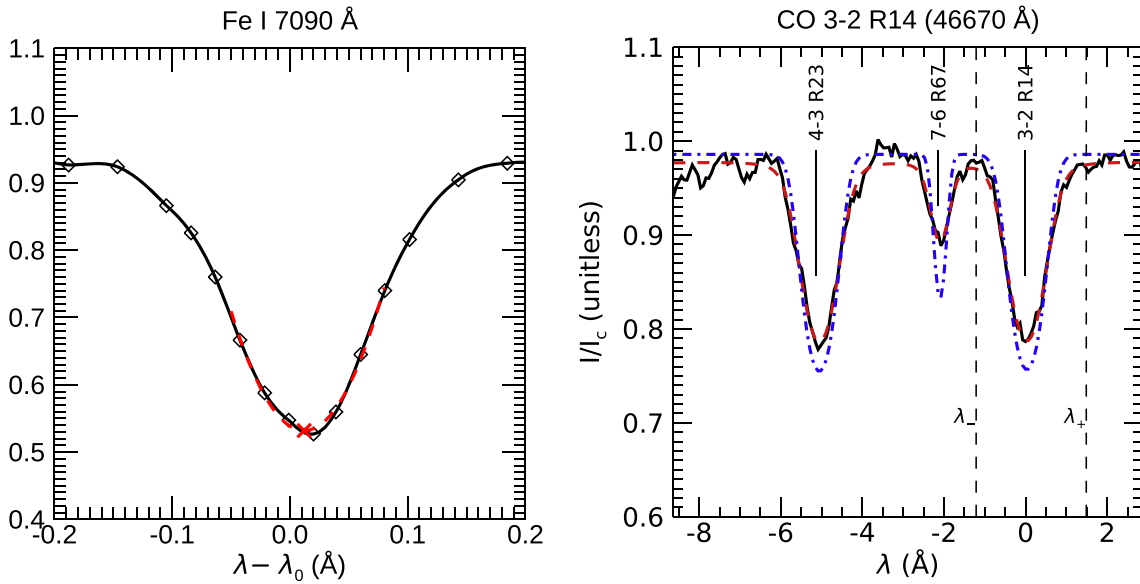
Figure 4. Example parameter calculations from the observed spectra. Left: for the IBIS spectra, the line core velocity and intensity (red X) are defined as the vertex of a parabolic fit to the line core (dashed red line). Right: for the NAC spectra, the equivalent width and line core velocity are calculated as moments of the spectral line between bounds $\lambda_{\pm}$ in the local continuum (vertical dashed lines, shown for the 3-2 R14 line). The line core intensity is calculated as for the IBIS lines. The spectrum shown has been corrected for variations in the flat field (approximated as a parabolic trend in the continuum level) and a constant scattered-light background. The Milne–Eddington model, accounting for the McMP/NAC spectral resolution, is shown by the dashed red line. The corresponding deconvolved model is shown by the dotted–dashed blue line.

2.3. Coalignment

The NAC scans were coaligned with the IBIS images by comparing the positions of the pore and several magnetic network elements, which appear clearly as bright features in maps of both the CO and Fe I 7090 Å line-core intensities observed by IBIS (see Section 2.2). A linear regression between the coordinates of these features in the IBIS and NAC reference frames yields an affine transformation that can be used to transform NAC scans into the IBIS coordinate frame and vice versa.

3. Methods

3.1. Spectral Line Parameters

For comparisons between the four spectral diagnostics (Na I D1, Fe I, Ca II, and CO), we calculated a set of standard line parameters. The line-minimum intensity I_0 and core wavelength λ_0 were extracted for each line by fitting a parabola to their cores, demonstrated in the left panel of Figure 4 for an example Fe I 7090 Å spectrum. For the CO line (which does not show appreciable asymmetry at the spectral resolution of the McMP spectrograph), a center-of-gravity measurement of

the central wavelength of the line is used instead to minimize uncertainty,

$$\lambda_0 = \int_{\lambda_-}^{\lambda_+} \left(1 - \frac{I_\lambda}{I_c}\right)\lambda d\lambda, \qquad (1)$$

where I_λ is the spectral line profile and I_c is the local continuum intensity (here, $\lambda_\pm$ are points in the continuum on either side of the spectral line, marked in the right panel of Figure 4 for the 3-2 R14 rovibrational line). The rest wavelength in both cases is taken to be the average core wavelength of the spectral line in the quiet Sun. The shift of λ_0 with respect to the line's rest wavelength can be used to calculate the Doppler shift of the spectral line, v_D. These parameters (I_0 and v_D) give information about the temperature and line-of-sight velocity in the solar atmosphere, respectively.

Additionally, the equivalent width of the CO line was calculated:

$$W_\lambda = \int_{\lambda_-}^{\lambda_+} \left(1 - \frac{I_\lambda}{I_c}\right)d\lambda. \qquad (2)$$

The equivalent width of a spectral line is a monotonic function of the column density of absorbers in the solar atmosphere. In the absence of a precise theoretical model for this dependence (the *curve of growth*, the calculation of which is beyond the scope of this paper), we treat W_λ as a qualitative proxy for the column density of CO in the atmosphere. While several CO lines are captured within the NAC spectral range, we focus here only on the 3-2 R14 transition, which is minimally blended with telluric and other CO lines, and the most evenly illuminated across the field of view.

3.2. Milne–Eddington Inversion of the CO Lines

Because the CO lines form in LTE (Ayres & Wiedemann 1989), their core intensities can be interpreted in terms of *brightness temperatures* (T_b) that reflect the gas temperature of the solar atmosphere at their heights of formation, which is necessary for the determination of chemical formation rates (Ayres & Rabin 1996). However, because the CO lines are so narrow their line core intensities are heavily influenced by the line spread function (LSF) of the McMath-Pierce spectrograph (which has insufficient spectral resolution to resolve the narrow CO lines, see Ayres (2003)) and scattered light. To account for these effects, we modeled the 3-2 R14 line (as well as the nearby 4-3 R23 and 7-6 R67 lines) using a Milne–Eddington model:

$$I_\lambda = S_0 + \frac{S_1}{1 + \eta_1\phi_1(\lambda) + \eta_2\phi_2(\lambda) + \eta_3\phi_3(\lambda)}. \qquad (3)$$

$S = S_0 + S_1\tau$ defines the source function of the solar atmosphere, η_i are the line strengths, and $\phi_i(\lambda)$ are Gaussian absorption profiles (which additionally depend on a Doppler shift v_{los} and a thermal broadening parameter $\Delta\lambda_D$, which may vary for each line). The ME model was convolved with the empirical LSF of the McMath-Pierce spectrograph (Ayres 2003) for direct comparison with the observed spectral profiles. For each observed spectrum, an optimal fit was found by varying the 11 model parameters (η, v_{los}, and $\Delta\lambda_D$ for each of the three spectral lines, plus S_0 and S_1 to define the source function)

through a Markov Chain Monte Carlo (MCMC) process. The model profile was then deconvolved with the LSF, and a constant scattered-light background was subtracted such that the depth ratio of the 3-2 R14 and 7-6 R67 lines matches the FTS IR atlas (Livingston & Wallace 1991). The absolute scale of these brightness temperatures is determined by assuming the continuum intensity to be the disk-center average brightness temperature of the 4.7 μm continuum, as an independent calibration of the temperature is not available for these observations. An example calculated ME spectrum is shown in the right panel of Figure 4, both with (red) and without (blue) degradation by the instrumental LSF.

4. Results

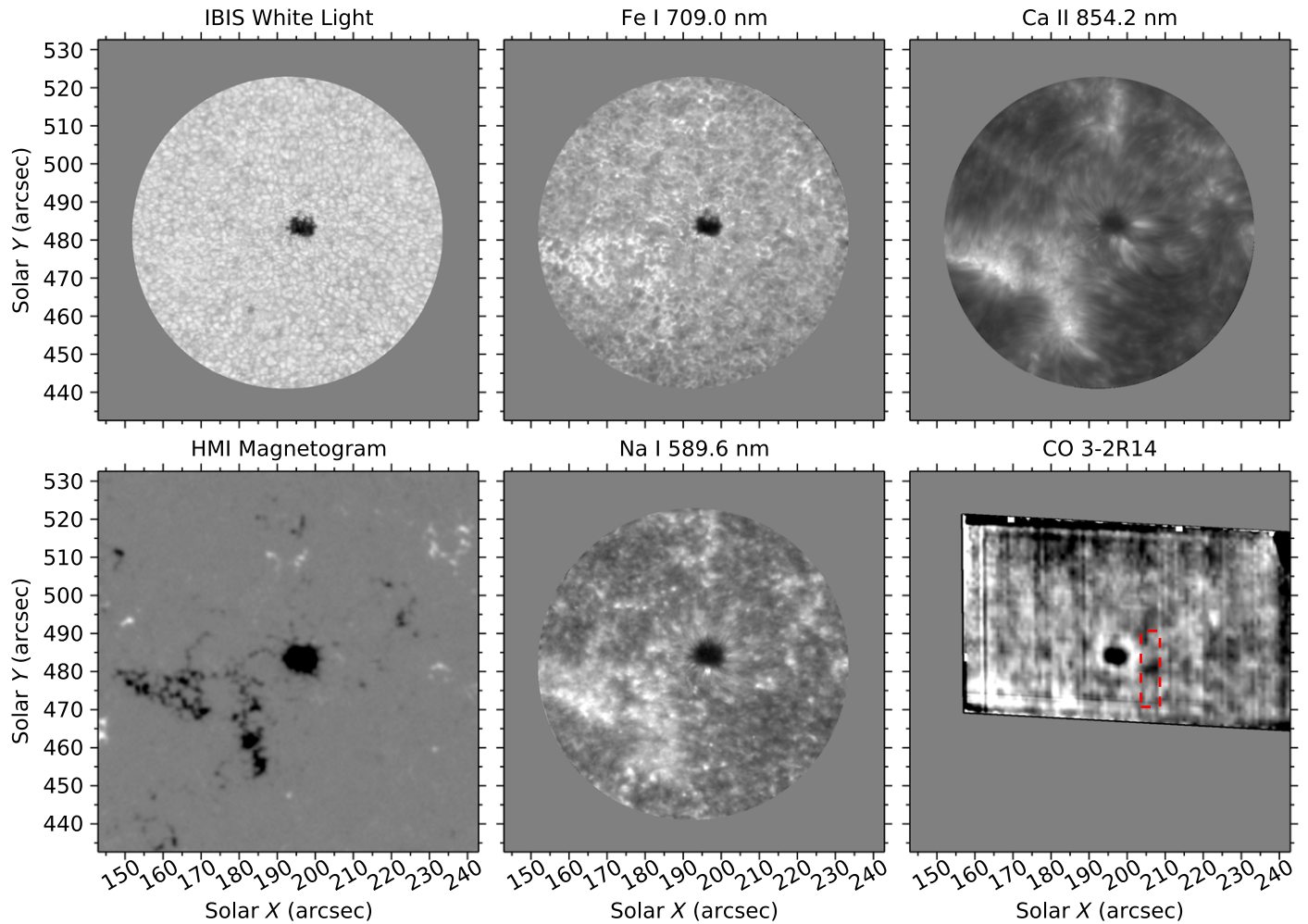### 4.1. Comparison of Line Core Intensities

By comparing the appearance of the solar surface as seen in the CO with the other spectral diagnostics (which have well understood formation characteristics), we can begin to piece together an understanding of the sensitivity of the CO absorption to various regions of the atmosphere. Figure 5 shows a representative example of the line core intensity of these spectral lines, as well as the visible continuum and HMI magnetogram.

Of the three lines observed by IBIS, Fe I 7090 Å forms the lowest, with its line core sensitive to the mid-photosphere. Therefore, its line core intensity is dominated by the 5 minute helioseismic oscillations and inverse granulation (Janssen & Cauzzi 2006), a pattern of dark granules separated by bright inter-granular lanes, which is caused by cooling from adiabatic expansion above the granular convective cells and the corresponding heating above the downflow lanes (Cheung et al. 2007). The plage and magnetic network appear bright (due to the higher magnetic pressure in these areas of concentrated field, which results in a lower density to maintain hydrostatic equilibrium and lowers the height of line formation), while the pore is dark due to the suppression of the solar convection by its strong magnetic field.

The formation of Na I D1 is more complicated, as its line core intensity is dominated by NLTE resonance scattering (Leenaarts et al. 2010). This causes the line core to be sensitive to a wide range of heights spanning the photosphere and lower chromosphere.

The line-core intensity images appear similar to those of Fe I 7090 Å, with a few notable differences. First, faint, elongated "penumbra-like" bright and dark filaments appear around the edge of the pore, due to the increased influence of the magnetic field on the plasma at its higher formation height. We also note that the bright spots corresponding to the plage and network are more diffuse than in Fe I; this is due to 3D scattering effects redirecting light emitted horizontally from their hotter, magnetized atmospheres into the line of sight, creating bright, diffuse "aureoles" surrounding these features (Leenaarts et al. 2010).

The highest-forming line observed by IBIS is Ca II 8542 Å. This line is sensitive to two regions: the shallow, LTE-dominated wings are sensitive to the mid-photosphere, while the NLTE line core is sensitive to chromospheric heights (for more detailed discussion, see Cauzzi et al. 2008). Because of this, the line-core intensity maps are dominated by elongated *fibrils* surrounding the pore and plage, which are the result of

Figure 5. Comparison of the line core intensities in the four observed spectral diagnostics. The left two panels show the IBIS white light reference (top) and HMI magnetogram (bottom). The line core intensities are shown for the photospheric Fe I and Na I lines (middle panels), and for the chromospheric Ca II line and the CO 3-2 R14 line (right panels), the latter of which forms in the temperature minimum. The IBIS scan shown here was captured between 17:35:46 UTC and 17:36:06 UTC, while the CO scan was captured between 17:34:54 UTC and 17:35:49 UTC. The red box denotes the region of the scan used to construct the spacetime diagram in Figure 6.

plasma being partially shaped by the inclined chromospheric *canopy field* in those regions. Where the photospheric magnetic field is concentrated, fibrils are mostly absent and the intensity is brighter and fairly uniform, typically indicating higher chromospheric temperatures.

The CO line-core intensity is most similar to the photospheric Fe I and Na I lines, with no large scale structures (e.g., fibrils) visible at the $\sim 1''$ sampling of the NAC observations, with the exception of the dark pore and bright plage/network. Previous observations of the CO spectrum taken in ideal seeing conditions (e.g., Uitenbroek 2000) show clear inverse granulation, corroborating this view of CO as a photospheric diagnostic. However, we note several features that appear in the CO line core but *not* the three atomic lines. First, we note the existence of several extended ($\sim 10''$–$20''$), dark regions to the north of the active region, with the strongest being to the northeast of the pore at $(X, Y) \sim (180, 515)$. While there is a visual similarity between these features and the "thermal shadows" seen by by Ayres (1998) in the vicinity of a sunspot pair (see his Figure 5), we note that these regions are confined to the northern edge of the field of view. This region is poorly illuminated on the detector, making measurements of the CO

line-core intensity there more susceptible to errors in the flat-field correction. Combined with the fact that these features rarely persist between consecutive scans, we believe that these regions of anomalously low intensity are most likely an artifact of the data reduction process. Second, we note that a bright "ring" is visible just surrounding the pore, showing brightness temperatures of ~ 4500 K, e.g., at $(X, Y) \sim (200, 485)$. A similar (albeit fainter) feature is seen surrounding the pore in the Na I image, indicating that this region of enhanced temperature may lie in the upper photosphere, where the lower-forming Fe I line is not sensitive. Last, we observe a small, dark region to the southwest of the pore ($(X, Y) \sim (205, 480)$) which is about $5''$ in diameter, with a brightness temperature of ~ 4000 K (compared to typical temperatures of 4200–4300 K in the quiet Sun). A spacetime diagram of the brightness of this feature (Figure 6) shows that it displays a persistent increase in equivalent width (top panel) and a simulteous depression of the CO line core intensity (bottom panel). These "cold bubbles" appear to be regions of CO-rich gas in the solar atmosphere and will be discussed in more depth in Section 4.3.
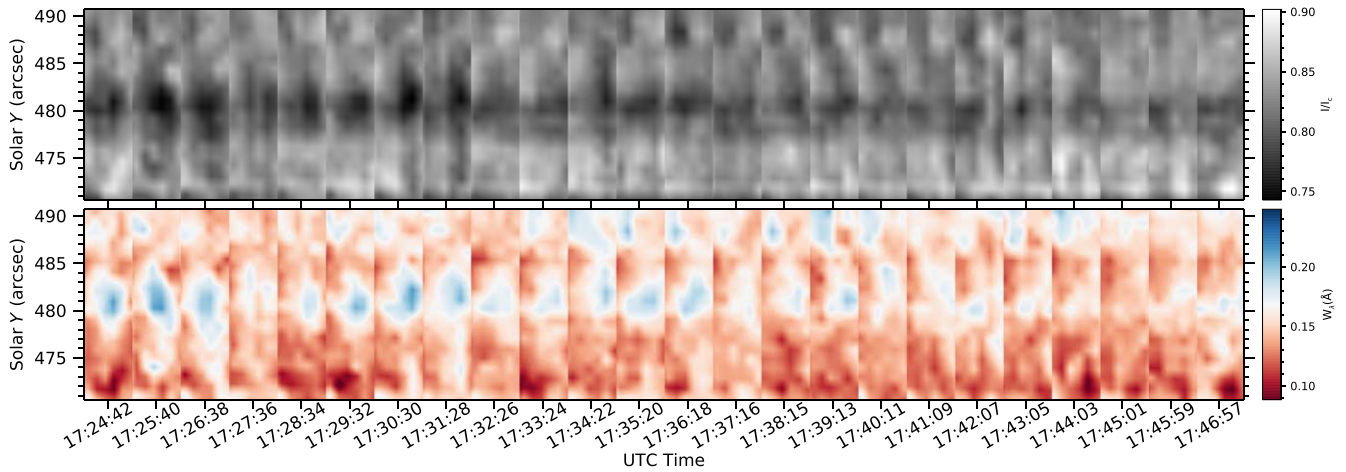
Figure 6. A spacetime diagram showing both line core intensity (top) and equivalent width (bottom) of an anomalous absorption feature (termed a "cold bubble") found to the southwest of the pore. Each slice of the plot shows a ∼5″ × 20″ rectangular region surrounding the bubble (denoted by the red contour in Figure 5).
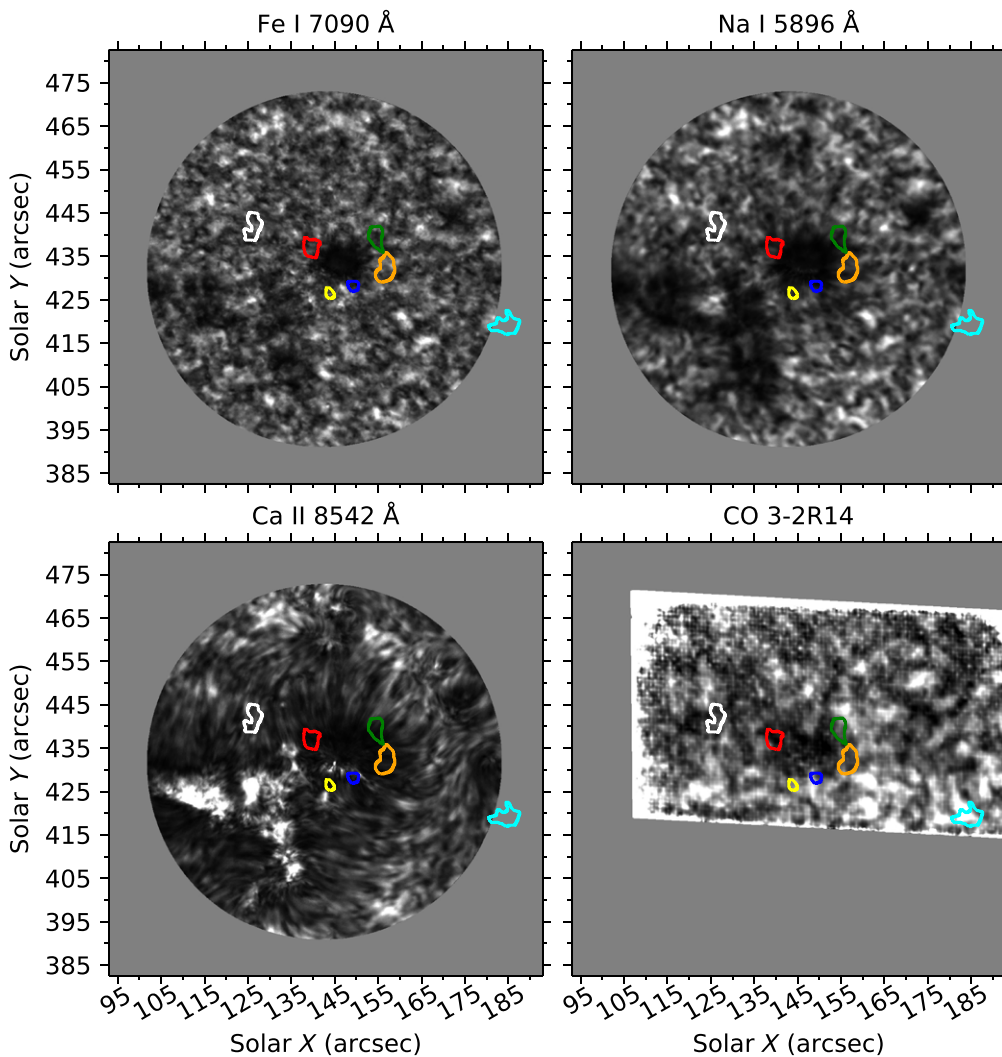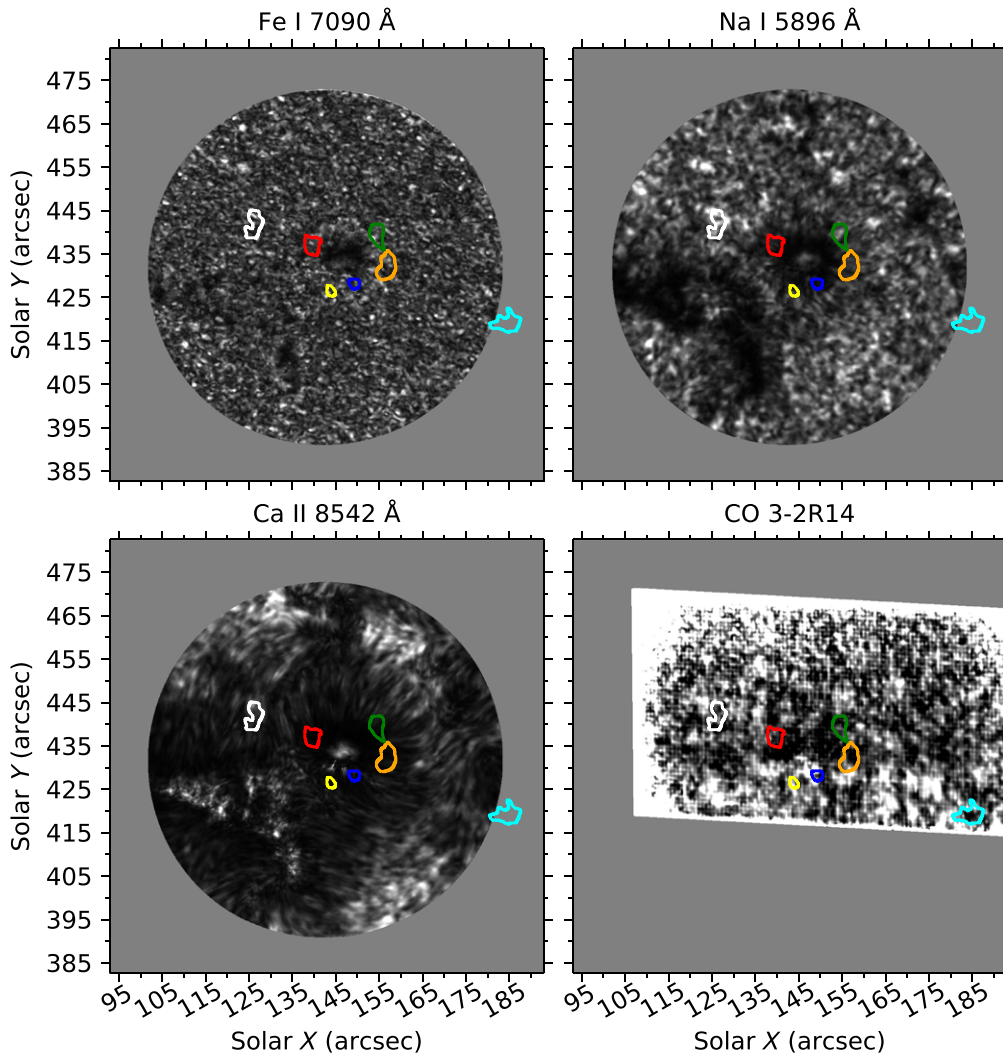

Figure 7. Maps of the 5 minutes (3.5 –5.5 mHz) power in the Doppler velocity of each spectral line. The 5 minute band corresponds to the dominant helioseismic oscillations in the photosphere. The colored contours show the locations of the eight "cold bubbles." The bright edges in the CO maps are due to higher noise levels in those boundary regions.

4.2. Comparison of Velocity Power Spectra

In addition to showing different features in their line core intensities, these spectral diagnostics in the visible show varying signatures of acoustic wave propagation in their Doppler velocity signals, shown in Figures 7 (for the 5 minute band, corresponding to photospheric helioseismic oscillations)

Figure 8. Maps of the 3 minute (5.7 mHz − 7.7 mHz) power in the Doppler velocity of each spectral line. The 3 minute band measures the power in frequencies just above the acoustic cutoff $\omega_c \approx 5.5$ mHz. The colored contours show the locations of the eight "cold bubbles."

and 8 (for the 3 minute band, corresponding to frequencies above the acoustic cutoff). These power maps were calculated for the 236 scans between 17:23 and 18:45 for the IBIS lines, and the 99 scans taken between 17:28 and 19:04 in the CO lines. In the lines that are sensitive to the lower layers of the solar atmosphere (Fe I 7090 Å and Na I D1), the 5 minute power is roughly isotropic across the field of view, except for a slight depression around the pore and plage. In Ca II 8542 Å, which forms above the height where low-frequency acoustic waves are reflected, the 5 minute power is enhanced in the plage relative to the quiet Sun.

The differences in the 3 minute power are more pronounced; while still isotropic in the quiet Sun regions of the field of view for the photospheric lines, there is a region of depressed power (termed the "magnetic shadow" by Vecchio et al. 2009) surrounding the pore and plage. The extent of this depression varies between the lines: it is nearly non-existent in the low-forming Fe I line, larger in the intermediate Na I D1, and largest in the high-forming Ca II line. In Ca II 8542 Å, the shadow coincides with the area covered by fibrils in the Ca II line-core intensity (compare to Figure 5). Additionally, we note that the shadow in Na I D1 may be slightly weaker in the region between the pore and plage (southeast of the pore).

Spatial variations in the CO velocity power are harder to discern due to the poorer spatial resolution and seeing conditions of the NAC observations. However, a few similarities with the IBIS power maps can be found. In maps of the 5 minute power, the CO observations seem most similar to the Fe I and Na I power maps, with a fairly isotropic pattern of power in the quiet Sun (however, unlike in those lines, there is not an apparent depression in the portion of plage that is visible in the CO scans). A magnetic shadow can also be seen surrounding the pore in the CO 3 minute power map, although it is more tenuous than in the IBIS lines (perhaps due to the poorer quality of the CO observing sequence). However, we note that it shows a similar anisotropy to the Na I D1 shadow, showing a lesser depression (or perhaps no depression) of acoustic power to the southeast between the pore and the plage.

Additionally, for each cospatial pixel, we calculated the Fourier *phase spectra* of these lines, shown in Figure 9. Each panel contains a 2D histogram, independently for each frequency bin (horizontal axis) showing the relative frequency of a given phase shift (vertical axis) between the Doppler velocity time series of two selected spectral lines. The red curve in each panel represents the peak of the phase shift distribution for each frequency bin, determined through a Gaussian +
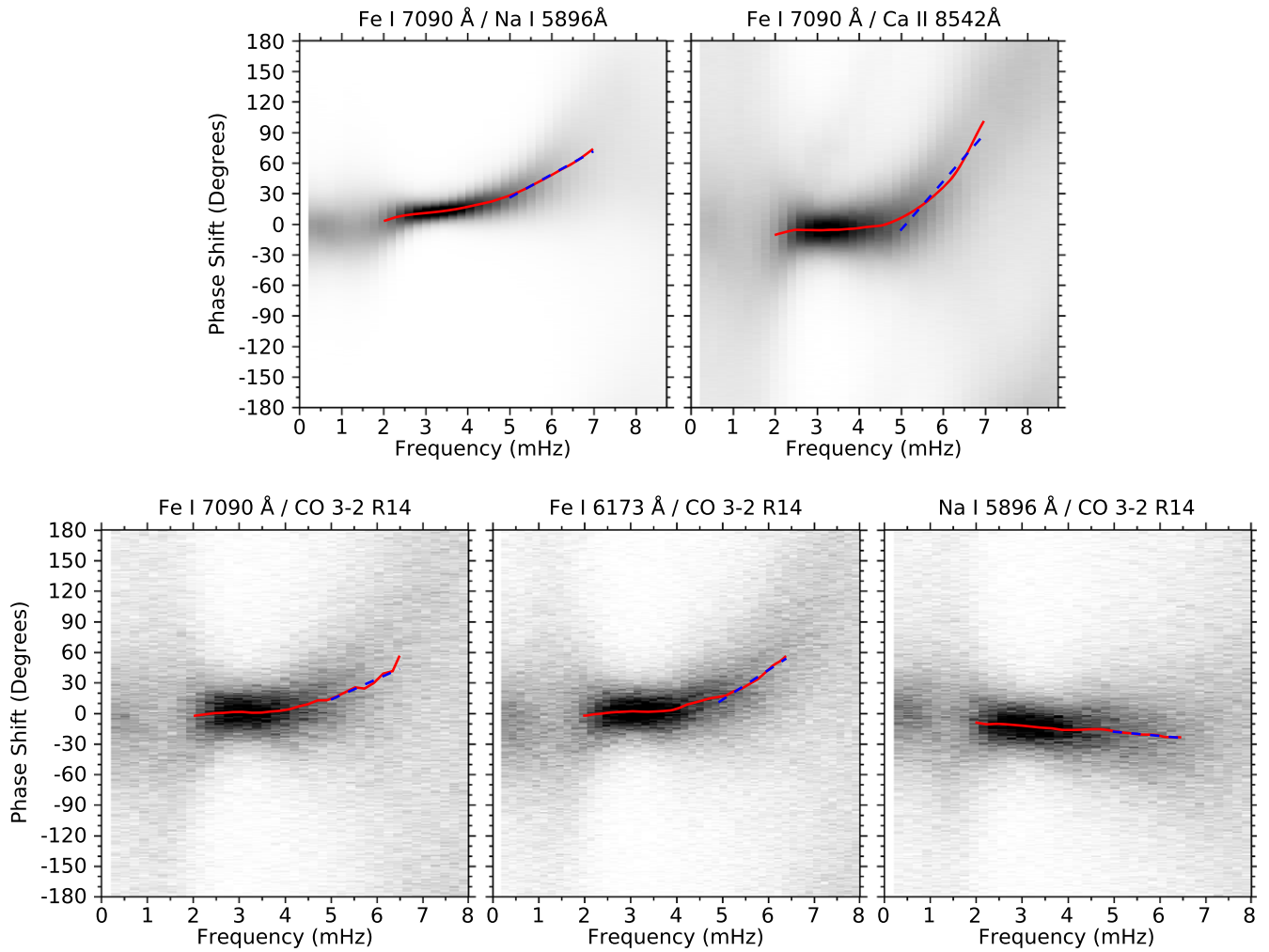
Figure 9. Doppler velocity phase spectra between the various observed spectral lines. The shading represents a histogram of the observed phase shifts in each frequency bin, while the red line shows the peak of the distribution at each frequency. The dashed blue line represents a linear fit to the phase-frequency trend in the 5–7 mHz (for the IBIS spectra in the top row) or 5–6.5 mHz range (for the CO spectra in the bottom row). Top row: the spectra of Na I 5896 Å (left) and Ca II 8542 Å (right) with respect to Fe I 7090 Å. Bottom row: the spectra of CO 3-2 R14 with respect to Fe I 7090 Å (left), HMI Dopplergram (center), and Na I 5896 Å (right).

constant fit to the 1D histogram (which is a more robust measure than the mode, especially for the noisier CO phase spectra in the bottom row). The curve is only shown for the range of frequencies where the phase spectra are coherent, 5–7 mHz for the atomic phase spectra (top row) and 5–6.5 mHz for the noisier CO spectra (bottom row). Note that, in order to create the phase spectra between the CO line and the other diagnostics (which were measured at a different resolution and cadence), the data were resampled to match the spatial resolution and cadence of the NAC scans. The resultant time series were trimmed to contain only time steps where velocity data is available for both diagnostics: 82 scans taken between 17:24 and 18:43 for the NAC/IBIS spectra, and 99 scans taken between 17:28 and 19:04 for the NAC/HMI spectra.

Examining the phase difference between Fe I 7090 Å and Na I D1 (top left) and Ca II 8542 Å (top right) as a function of frequency, we see two distinct regions. First, at lower frequencies ($\sim$2–5 mHz), the phase curve is flat, and the phase difference between the lines is near zero. At higher frequencies, ($\sim$5–7 mHz) the phase difference increases approximately linearly with frequency. A similar trend can be seen in the between CO 3-2 R14 and Fe I 7090 Å (bottom left)

Table 1
Measured Slopes of the Phase-frequency Trend for the Various Phase Spectra in Figure 9

Line # 1	Line # 2	Slope (Radians/Hz)
Fe I 7090 Å	Na I 5896 Å	398
Fe I 7090 Å	Ca II 8542 Å	827
Fe I 7090 Å	CO 3-2 R14	352
Fe I 6173 Å	CO 3-2 R14	502
Na I 5896 Å	CO 3-2 R14	−71.8

(although the spectrum is noisier on account of the sparser spatial sampling of the NAC scan), as well as with the HMI dopplergram, which utilizes the photospheric Fe I 6173 Å line (bottom center). In comparison, the phase spectrum with respect to Na I D1 (bottom right) is much flatter, with a slight negative slope above the acoustic cutoff. These non-zero slopes (blue dashed lines, values recorded in Table 1) will be discussed in Section 5.3, where we will use them to estimate the relative formation heights of these lines.
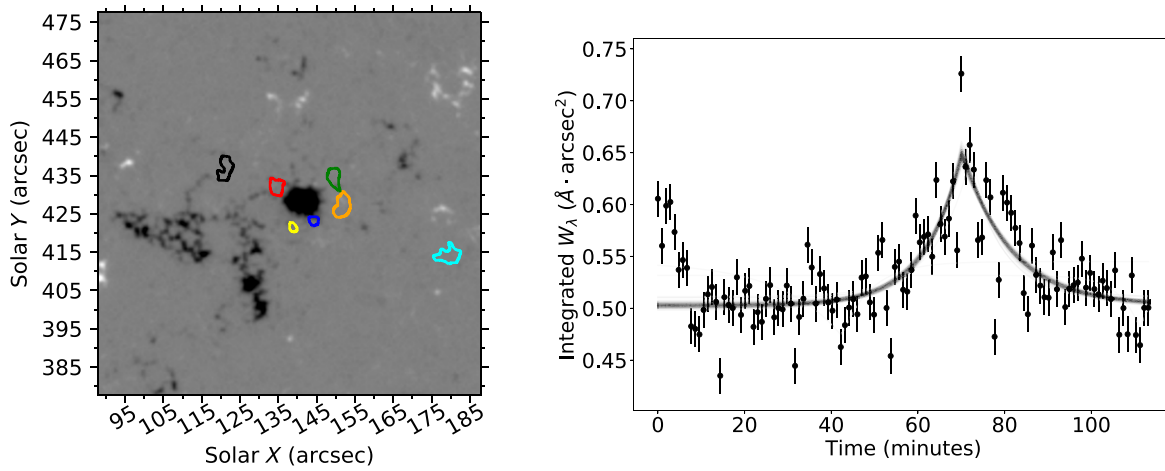
Figure 10. Locations of the seven detected cold bubbles, shown in relation to the HMI magnetogram from Figure 5 (left). A plot of the total equivalent width in one bubble (right), with sample MCMC model curves shown in black. Error bars indicate the uncertainty in each measurement of the integrated equivalent width, propagated from the uncertainty in the CO spectral profile.

4.3. Epoch Analysis of Cold Bubbles

For the purposes of this paper, we define a "cold bubble" to be a region that displays at least a 2σ enhancement in its CO equivalent width for five or more consecutive NAC scans (approximately 5 minutes). This technique allows for the detection of persistent features with significant amounts of CO relative to the solar background. During the observing sequence, seven such features were detected (shown in Figure 10). Note that these features are clearly not evenly distributed across the field of view. Instead, most of them are clustered around the boundary of the pore; only two are located in what might be considered quiet Sun (despite such regions covering ~90% of the field of view). To assess the evolution of these features, we performed an *epoch analysis* of their evolution. As a proxy of the total amount of excess CO in each bubble, we calculated the area-integrated equivalent width within its boundary (defined by the contours shown in Figure 10) in each scan. The resulting curves (one of which is shown in the right panel of Figure 10) were then fit to an exponential model curve:

$$W_{\text{tot}}(t) = W_0 + A \times \begin{cases} 2^{(t-t_0)/\tau_+} & t < t_0, \\ 2^{-(t-t_0)/\tau_-} & t > t_0, \end{cases} \quad (4)$$

where W_0 represents a constant "background" equivalent width, A is the amplitude of the excess signal, t_0 is the time where the signal peaks, and $\tau_{\pm}$ are the doubling time (for the rise phase) and the half-life (for the decay phase) of the bubble, respectively. This model was chosen as the simplest self-similar model for the observed behavior, since self-similarity is implicitly assumed during the renormalization step of the analysis. The four model parameters were calculated for each bubble using a MCMC process to ensure convergence to a global minimum solution. These parameters were then used to combine the eight individual curves into a single *epoch curve*, defined to have unit amplitude and to peak at $t = 0$. The epoch curve was fit by the same model to estimate characteristic values of $\tau_{\pm}$ that describe the collective behavior of the bubbles (see Figure 11 for the results of this analysis).

Physically, this can be interpreted as a manifestation of self-catalytic CO formation (the "molecular cooling catastrophes"

of Ayres & Rabin (1996), described there as a mechanism to enforce the thermal bifurcation of the chromosphere into a two-component atmosphere). This behavior arises from two things: the strong radiative cooling provided by the IR CO spectrum and the sensitivity of CO formation to temperature. Consider a region where CO radiative cooling dominates the local energy balance of the solar atmosphere. This region will have heightened radiative losses from CO spectral emission, leading to a decrease in temperature with a cooling rate proportional to the density of CO. This decrease in temperature causes an increase in CO density, thereby increasing the cooling rate. That is, the sensitivity of the CO density to temperature creates a situation where the rate of cooling (i.e., the rate of change of temperature) is proportional to the temperature, creating exponential cooling of the atmosphere. On the contrary, if CO cooling does not dominate the local energy balance (e.g., there is an external source of heating), the reverse will happen: the atmosphere will heat up, causing the CO concentration to decrease, which lowers the rate of radiative cooling and causes the atmosphere to heat more quickly. This behavior was demonstrated by Anderson & Athay (1989), who calculated 1D temperature profile of the solar atmosphere under various levels of prescribed heating. Their Figure 1 shows that, below a critical level of heating, the chromosphere can be cooled down to 3000 K by molecular CO (similar results can be seen in Figure 4 of Wedemeyer-Böhm & Steffen 2007). However, at higher levels of heating, the solar atmosphere exhibits a hot chromosphere. Therefore, the growth phase of our exponential model represents the evolution of an atmosphere where the local acoustic heating has somehow been dampened, allowing for exponential formation of CO. The acoustic heating surpasses the critical value at t_0, leading to the exponential destruction of the CO until it reaches its baseline, equilibrium level.

We note that our model does not aim to describe the small-scale variations of the individual equivalent width curves (such as the effect of the 5 minute oscillations) which leads to a large amount of scatter in the epoch data set which cannot be explained by the propagated uncertainty in the equivalent width measurements. Therefore, fitting the simplified model given by Equation (4) to this data produces a solution with an undesirably large goodness-of-fit metric ($\chi^2 = 23$). The scale
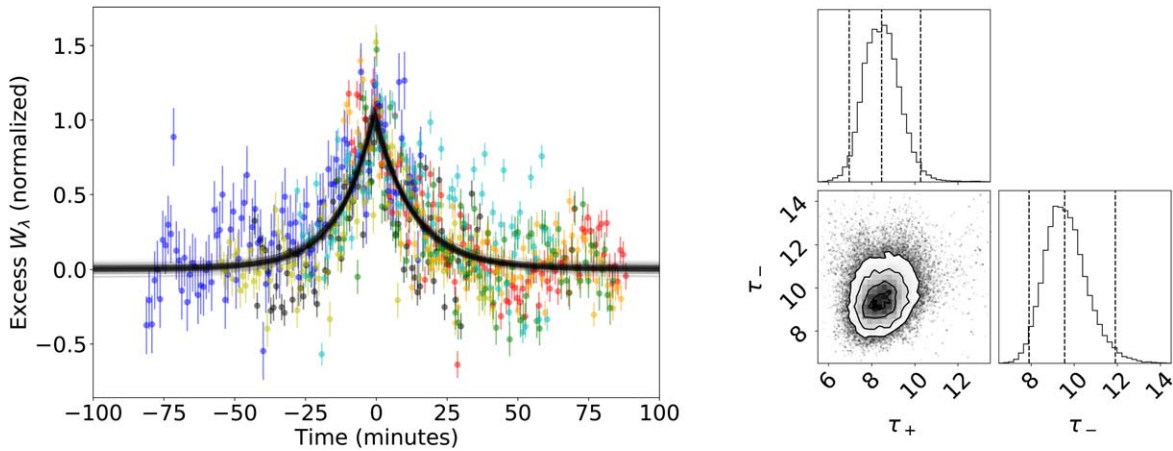
Figure 11. Results of an epoch analysis of the "cold bubble" evolution. Left panel: a plot of the normalized, coaligned excess equivalent width seen in each "bubble" (dots, color-coded to match the "bubble" contours seen in Figure 10). Error bars denote the 2σ uncertainty in each measurement, propagated from the uncertainty in the measured CO spectral profiles. Black lines show a sample of MCMC model fits to the data. Right panel: a corner plot showing the covariance of the estimates for τ_+ and τ_-. The solid contours in the scatterplot represent the 68%, 95%, and 99% confidence intervals for the bivariate distribution. The top and right plots show the univariate distributions for τ_+ and τ_-, where the dashed lines show the median and 95% confidence intervals for each distribution.

separation between the unmodeled effects and the long-term evolution of the bubble ensures that the best-fit model parameters should not be biased by this non-random error—however, the MCMC parameter uncertainties returned by such an approach would be underestimated. Therefore, we chose to artificially scale the uncertainties used in the calculation of the MCMC χ^2 objective function such that the best-fit model has $\chi^2 = 1$. This allows us to retrieve more appropriate estimates of the uncertainties for the fitted lifetimes of the rise and decay phases.

Examining the epoch curve (the left panel of Figure 11), we note that the seven normalized bubble curves fit together well into a cohesive exponential profile, justifying our choice of a self-similar model, and that they appear to be well described by the ensemble of MCMC model fits. Examining the bivariate distribution of τ_+ and τ_- (right panel), we see that the estimates of these two parameters are uncorrelated (i.e., independent), with values of $\tau_+ = 8.4^{+1.8}_{-1.5}$ minutes and $\tau_- = 9.6^{+2.3}_{-1.7}$ minutes, respectively. A physical interpetation of these time scales in terms of a formation height will be presented in Section 5.4.

5. Discussion

5.1. Comparison of Diagnostics

While similarities can be found between the CO spectra and various features of the Fe I 7090 Å, Na I 5896 Å, and Ca II 8542 Å lines, the CO 3-2 R14 line shows several unique features indicating the 4.7 μm band as an additional spectral region to study the dynamic solar atmosphere, in addition to other traditional diagnostics of the photosphere and chromosphere.

First, the region surrounding the pore shows a bright ring corresponding to an area with an increased brightness temperature of $T_b \approx 4500$ K. This feature is not seen in observations of fully developed sunspots (see, e.g., Uitenbroek et al. 1994; Ayres 1998; Li et al. 2020), suggesting that its presence may be related to the ongoing decay of this active region or its lack of penumbra. The elevated temperature of this region may indicate a source of heating at the boundary of the pore, such as Joule heating or the dissipation of MHD waves (Stangalini et al. 2021). Since a similar feature is not visible in

Fe I 7090 Å or Ca II 8542 Å, this heating would need to be localized to the middle atmosphere. We note that a similar, albeit weaker, brightening is visible in the Na I D1 core intensity, however, while the interpretation of Na I D1 is complicated by NLTE scattering effects (Leenaarts et al. 2010), the CO line is believed to form in LTE (Ayres & Wiedemann 1989). Therefore, the CO lines are a useful diagnostic of the local temperature in this region.

Alternatively, this brightening could be caused by the concentration of small-scale magnetic features surrounding the pore, which may affect the CO line core intensity similarly to the magnetic network. However, this explanation seems less likely; any such features would need to exist below the 0″.6 resolution of the HMI magnetogram while still effecting a 200–300 K in the CO brightness temperature (similar to the much stronger plage field). Further analysis (especially of data at higher spatial resolution) would help rule out this possibilty.

The CO lines also show several long-lived, transient episodes of excess absorption we have termed "cold bubbles." These events, which may last as long as 30–40 minutes, are characterized by diminished brightness temperature and increased equivalent width (i.e., column mass), relative to the quiet Sun, in an area as large as 5″ in diameter. This paper marks the first study of such features, which have not been emphasized in previous studies. Sparse references to unexplained "cooling events" (lasting up to 10 minutes) in the quiet Sun have been reported (e.g., Ayres & Rabin 1996), but no events of the magnitude or longevity seen here have been reported. It is possible that these two phenomena may be related (e.g., that the cooling events observed by Ayres & Rabin (1996) are short-lived, quiet Sun analogues of the "cold bubbles" analyzed here). The few studies of CO around magnetically active regions (e.g., Ayres 1998; Uitenbroek 2000) did not report seeing any such transient cooling events, likely because they lacked the temporal resolution to observe the evolution of these features. More recently, preliminary observations of the CO 4.7 μm spectrum by GST/CYRA (Yang et al. 2020) showed several "unusual absorption features" in the vicinity of a solar pore and its surrounding plage (see their Figure 9 and the related discussion in Section 3.2). We believe that these may be examples of

"cold bubbles," although it is not possible to make an umambiguous identification from the single raster scan presented by the authors.

5.2. Power Spectra

In Section 4.2, we noted that the majority of the observed "bubbles" appear near the boundary of the pore, where the magnetic canopy field inhibits the transmission of acoustic power into the chromosphere. Therefore, the presence of the canopy field seems to be an important (although not strictly necessary) factor in their formation. This suggests that the "cold bubbles" may be of chromospheric origin—simulations of CO formation using CO5BOLD (Wedemeyer-Böhm et al. 2006; Wedemeyer-Böhm & Steffen 2007) found that, while CO is abundant in the photosphere, heating from acoustic shocks in the non-magnetic Sun prevents the formation of significant CO at chromospheric heights.

Therefore, in order to facilitate the formation of high-altitude CO bubbles, the canopy field might inhibit the acoustic heating of the atmosphere surrounding the pore, such as from acoustic shocks. While it is difficult to confidently identify shocks in the region near the pore (since their decreased amplitude makes them difficult to distinguish from non-shocking velocity perturbations), Vecchio et al. (2009) found a correlation between the integrated 3 minute power in Ca II 8542 Å and the summed shock amplitude observed in that line; therefore, we treat the 3 minute power as a proxy for shock heating around the pore.

As noted in Section 4.1, a "magnetic shadow" of depressed 3 minutes power is seen surrounding the pore in all four spectral lines, appearing stronger and more extended in the higher-forming lines, where the field has spread out from the pore and become more inclined. The extent of the shadow in each spectral diagnostic can easily be seen by examining the radially averaged 3 minutes power surrounding the pore, as shown in Figure 12. We note that the five "bubbles" that surround the pore (colored shaded regions) lie well within the boundaries of the shadow, where the 3 minute power is only 60%–70% of its quiet Sun value in the CO line (and even lower in Na I and Ca II).[4]

5.3. Phase Spectra

The slope of the phase spectra displayed in Figure 9 can be understood by considering the source of velocity power at low (<5 mHz) and high (> 5 mHz) frequencies in the solar atmosphere. The sub-5 mHz power is due primarily to helioseismic oscillations: resonant wave modes trapped from below by the density gradient in the solar interior and from above by acoustic reflection by the rarefied upper atmosphere. The majority of the power in these frequencies is in standing wave modes, which oscillate in phase at all heights; therefore, the phase spectrum between any two lines should be zero below the acoustic cutoff frequency. Above this frequency, power is instead carried by traveling waves, which results in an increasing trend in the phase delay between more widely separated heights. Taking the simplified case of a vertically propagating plane wave, the phase difference

---

[4] We note that the amplitude of the power depression surrounding the pore in the CO line may be underestimated due to the higher noise floor of the CO power spectra and the fact that the 3 minutes power band is much closer to the Nyquist limit for the NAC observations than the IBIS sequence.
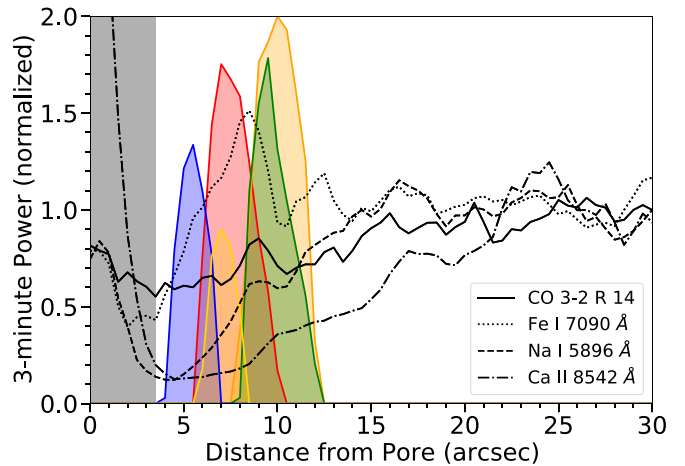
Figure 12. The radially averaged 3 minutes power surrounding the pore observed in CO (solid), Fe I 7090 Å (dotted), Na I 5896 Å (dashed), and Ca II 8542 Å (dotted–dashed). All four curves have been normalized to their relative average quiet Sun power between 23″ and 30″ from the pore, where the radial trend in power is relatively flat in all four lines.. The gray shaded region represents the extent of the pore itself, while the colored shaded regions show the locations of the five bubbles surrounding the pore (color-coded to match Figure 10). Taller/wider peaks correspond to larger "bubbles."

between the velocity oscillations of at two heights separated by a distance Δz (representing the regions of sensitivity for two different spectral lines) depends on the wave number k of the wave:

$$\Delta\phi = k\Delta z \approx \frac{2\pi\nu}{c_s}\Delta z, \tag{5}$$

where ν is the wave frequency and the sound speed is c_s. Here, we see that $\Delta\phi \propto \nu$, explaining the linear phase curve above the acoustic cutoff frequency. Solving for Δz, we have

$$\Delta z \approx \frac{\Delta\phi}{\nu}\frac{c_s}{2\pi}. \tag{6}$$

Therefore, Δz is directly proportional to the slope of the phase spectrum (measured in radians/Hz). For the measured slopes listed in Table 1 and assuming a nominal sound speed of $c_s = 7\,\mathrm{km\,s^{-1}}$, we find that $\Delta z = 440\,\mathrm{km}$ for the Fe I—Na I phase spectrum and $\Delta z \approx 920\,\mathrm{km}$ for the Fe I—Ca II spectrum. Given the formation height of Fe I 7090 Å is approximately 250 km (e.g., as synthesized in the FAL-C model atmosphere; Fontenla et al. 1993), we estimate that Na I D1 and Ca II 8542 Å form at ∼ 690 km and ∼ 1200 km, respectively, consistent with radiative transfer modeling of these lines.

Although the phase spectrum between Fe I and CO is noisier than the Na I and Ca II spectra, the same analysis produces a height difference of 390 km, indicating a formation height of ∼ 640 km. This is near the top of the temperature minimum region and slightly lower than the formation height of Na I D1. This is supported by the slightly negative slope in the Na I—CO phase spectrum. An independent measure of the CO formation height can be derived from the HMI phase spectrum, which indicates a height difference of 560 km. Fe I 6173 Å forms at around 100 km (Fleck et al. 2011), giving a CO formation height of 660 km, consistent with the other measure. Using the same analysis, the formation heights of three other

strong CO lines were calculated to be 570 km (4-3 R23), 660 km (2-1 R06), and 530 km (6-5 R46).[5]

While this is the first time the CO formation height has been measured directly using velocity phase differences ($V - V$ phase spectra), a related approach was used by Penn et al. (2011) to estimate the average formation height of the several strong CO lines.[6] The authors measured the average phase difference between the velocity and intensity fluctuations in the CO spectrum (the $I - V$ phase spectrum). By comparing the observed phase difference in these lines to those tabulated for the IR continuum from 50 μm to 800 μm (Kopp et al. 1992), the CO lines were estimated to form from 425 km at disk center to 560 km at $\mu = 0.5$. At $\mu = 0.9$ (comparable to our observations), this analysis implies the CO lines should form at $z \approx 450$ km, significantly lower than our estimates. This difference could be due to several factors. First, the IR continuum phases provided by Kopp et al. (1992) are only given at a handful of wavelengths, and are quite uncertain at the $\sim$ 400–500 km heights inferred for the CO lines by Penn et al. (2011). Additionally, the IR continuum formation heights quoted by Kopp et al. (1992) are derived from the VAL-C semiempirical model atmosphere (Vernazza et al. 1981), an ancestor of the FAL-C model, and may not be suitable for interpreting the formation height of spatially resolved IR spectral lines. Accounting for these sources of uncertainty, the observed difference between the $I - V$ and $V - V$ estimates of the CO formation heights may not statistically significant.

Additionally, when the authors used the analytical model presented by Kopp et al. (1992) (which uses Newton's cooling law to account for deviations from adiabatic cooling of the atmosphere) to model the frequency-dependent $I - V$ phase shift of their data, they found that they needed longer cooling time scales for CO than were needed by Kopp to reproduce the phase shifts in the IR continuum. Since Kopp found that the non-adiabatic cooling timescale of the solar atmosphere increases with height, this could imply that the CO lines form higher in the atmosphere than the average $I - V$ phase analysis suggests (perhaps more in line with our estimates). Alternatively, it may suggest that the non-adiabatic cooling mechanism introducing the $I - V$ phase shift in the CO spectrum (most likely radiative cooling from the CO lines themselves) differs from that observed in the IR continuum, complicating a straightforward interpolation of the CO formation height from the IR continuum phase shifts.

5.4. Cold Bubbles

First, we address whether the "cold bubbles" described in Section 4.1 are similar to phenomena already described in the literature. In a study of the quiet Sun, Uitenbroek (2000) found that the variation of the quiet Sun CO brightness temperature could be decomposed into two components: (1) the 5 minute helioseismic oscillations (which act on spatial scales of several arcseconds, but at time scales of 5 minutes, much shorter than observed here), and (2) the solar granulation (which evolves on a timescale of $\sim$ 10 minutes, but on spatial scales that are not resolved by McMP/NAC except in excellent seeing conditions). The scale separation between these processes and the observed spatiotemporal scales of the "cold bubbles" means

that these features are likely not related to those phenomena. Supporting this conclusion, we note that both the 5 minute oscillations and the solar granulation are ubiquitous in the photosphere, meaning that if they directly caused the "cold bubbles," we would expect to see bubbles occur more uniformly within the field of view. The fact that these features instead appear almost exclusively around the pore (despite it filling only a small portion of the target region) suggests that they may originate in the chromosphere, where the magnetic field can more substantially influence the atmosphere and serve to differentiate the region surrounding the pore from the rest of the quiet Sun.

This hypothesis is supported by examining the evolutionary time scales $\tau_{\pm}$ of the bubbles (obtained through the epoch analysis performed in Section 4.3) in relation to the chemical evolution of CO in the solar atmosphere. If we assume that the formation of these bubbles is mediated primarily by chemical processes, we can equate the measured values of $\tau_{\pm}$ with the chemical formation timescale of CO (Ayres & Rabin 1996), which scales with the temperature T and neutral hydrogen density $n_{\rm H}$ of the solar atmosphere:

$$t_{\rm CO}^{\rm chem} \approx 0.5 \left(\frac{T}{5000 \text{ K}} \right)^{-16.2} \left(\frac{n_{\rm H}}{1 \times 10^{15} \text{ cm}^{-3}} \right)^{-1} \text{s.} \qquad (7)$$

Assuming a nominal temperature of 4000 K (the approximate temperature of the cold bubble in Figure 5, obtained from ME inversion) and assuming a timescale of 7 minutes (on the lower end of our confidence intervals), we can estimate the density of the solar atmosphere in the vicinity of the "cold bubbles" to be about $n_{\rm H} \approx 4.4 \times 10^{13} \text{ cm}^{-3}$. In the FAL-C atmosphere (Fontenla et al. 1993), this corresponds to a height of $z \approx 970$ km. We note that this is a lower bound on the bubble's height in the solar atmosphere, since longer time scales indicate lower densities. For example, a timescale of 12 minutes (the upper end of the range of uncertainties) corresponds to an altitude of 1040 km. These height estimates differ slightly based on the atmospheric model being used. For example, the noted time scales imply a range of heights from $\sim$ 930–990 km using the cooler FAL-A model, and $\sim$ 1000–1070 km in the hotter FAL-F model.

No matter which model is used, these results generally agree with the observed limb extensions of the 3-2 R14 line (Solanki et al. 1994). This reinforces the idea that these "cold bubbles" may be manifestations of chromospheric CO viewed on-disk. However, these heights differ significantly from the formation heights inferred for the quiet Sun from the phase-difference spectra in Section 5.3. This implies that, if these features are ubiquitous in the quiet Sun (as they must be, to produce the observed extensions everywhere above the solar limb), they must represent a tenuous, minority component of solar CO, which is overpowered by the absorption from photospheric CO near disk center, but may become visible near the limb due to the elongated sight line through the chromosphere. Therefore, the "cold bubbles" discussed in this paper may represent a unique opportunity to study the temporal evolution and spatial distribution of chromospheric CO on-disk. It is possible that observations with improved spatial and spectral resolution may be able to detect signatures of more tenuous "bubbles" in the quiet Sun that were not visible in the McMP/NAC data analyzed here.

---

[5] A reliable phase spectrum for the 5-4 R33 line was not able to be calculated, as it is heavily blended with the neighboring 7-6 R66 line.
[6] While the authors observed three lines (4-3 R23, 3-2 R14, and 2-1 R06), they averaged the parameters of the three lines to reduce noise.

6. Conclusion

6.1. Numerical Modeling

6.1.1. MHD Modeling of the Cool Chromosphere

Cold pockets of gas (possibly analogous to the "cold bubbles" observed here) can also be seen in various computational models such as recent simulations using BIFROST (Leenaarts et al. 2011), which show an abundance of ultra-cold (<2000 K) plasma extending as high as 2–3 km above the photosphere, although they are periodically disrupted by the passage of acoustic shocks. These results suggest that, in the absence of shock heating (such as in the magnetic shadow surrounding the pore), the chromosphere could easily reach temperatures low enough to form significant amounts of CO. However, BIFROST only treats molecular abundances in the instantaneous chemical equilibrium (ICE) approximation, which is not sufficient to study the concentration of CO in shocking atmospheres. Further studies of nonequilibrium chemistry using codes like CO5BOLD, especially in magnetized atmospheres, is needed in order to assess the effect of these cold pockets on observed CO spectra. By simulating CO formation in a variety of magnetic topologies, it will be possible to study the occurrence rates and distribution of these "cold bubbles" in more detail, informing the interpretation of these features.

6.1.2. Radiative Transfer of CO Lines

While several attempts have been made to model the formation height of the CO lines in one- or two-component semiempirical atmospheres (e.g., Avrett 1995; Ayres et al. 2006), treatments of CO line formation in 2D or 3D simulations of the solar atmosphere are less common. Uitenbroek (2000) simulated the formation of the two CO lines in a 3D hydrodynamic simulation of solar granulation (Stein & Nordlund 1998), assuming ICE. He found that the strong 3-2 R14 line forms at about 600 km (although in one small region with low CO density it forms as low as 150 km). However, the simulation used only extends for 500 km above the solar surface, with an additional 150 km isothermal "fiducial layer" at the top of the atmosphere to ensure an open boundary condition for the solar convection there. Since the CO line was found to form in this non-physical boundary layer, the formation height derived may not be accurate. Modern MHD simulations can reach much greater heights in the solar atmosphere (including the chromosphere and corona in some cases); therefore, repeating these analyses with modern simulation codes will allow for the more accurate determination of CO formation heights in a variety of solar structures and magnetic topologies.

6.2. New Observations

While these data mark the first on-disk observations of persistent, chromospheric, cooling events in the CO spectrum, we note that similar phenomena have been seen in other spectral diagnostics. Recent observations of the 3 mm continuum with the Atacama Large Millimeter Array (ALMA, Wootten & Thompson 2009) by Loukitcheva et al. (2019) showed extended regions of cold gas (referred to as "Chromospheric ALMA Holes," or ChAHs), which showed brightness temperatures as low as 4370 K. A similar phenomenon was observed in the 1 mm continuum (da Silva Santos et al. 2020),

which showed temperatures as low as 3000 K. By using this brightness temperature to constrain non-LTE inversions of the Mg II h & k doublet, the authors found that the low millimeter brightness temperatures implied the presence of narrow cold pockets in the chromosphere $\log \tau \in (-5, -5.5)$ (approximately, 900–1600 km in the FAL-C model). The response functions of strong CO lines like 3–2 R14 show similar sensitivities to the temperatures of these cool chromospheric regions as to the temperature minimum, implying that they may impact observed CO line profiles when they appear. The cool brightness temperatures seen in the ALMA bands have drawn comparison to the low-temperature sensitivity of the CO 4.7 μm, although it is unclear whether the phenomena seen in the two diagnostics are related. As shown here and elsewhere (e.g., Penn et al. 2011), the CO lines are primarily sensitive to the conditions at temperature minimum, especially when observed at the disk center, but they also be indicate the presence of cold regions higher in the atmosphere driven by the local dynamical conditions (e.g., the intermittent bubbles described in this work). On the other hand, the millimeter continuum is sensitive (on average) to the electron temperature (Wedemeyer-Böhm et al. 2007) at different heights depending on wavelength, although with a significant variability of local opacity (Martínez-Sykora et al. 2020) due to differences in the electron density. Because of this, the formation height of the millimeter continuum may vary significantly within the atmosphere (Loukitcheva et al. 2015) and inversions combining ALMA data with atomic lines indicate that the cold regions may come from lower in the solar atmosphere (Hofmann et al. 2021).

Therefore, while the "cold bubbles" observed in the CO spectrum and the ChAHs observed in the millimeter continuum may be manifestations of the same phenomena (e.g., chromospheric pockets of cool gas, as seen in BIFROST simulations, observed at different heights), coordinated observations between these diagnostics are needed to confirm this relationship. Although the McMath-Pierce Solar Telescope was decommissioned in 2018, two new IR spectrographs will soon provide new insights into the CO 4.7 μm spectrum. First, the new CrYogenic spectRogrAph at the Goode Solar Telescope (GST/CYRA, Yang et al. 2020), which began science operations in late 2021, is capable of observing these lines at a $\sim 0.''7$ spatial resolution with a spectral resolution of $R \approx 1.67 \times 10^5$, enough to fully resolve the cores of the CO lines (see Ayres 2003), a feat previously achievable only through Fourier transform spectroscopy (and hence limited spatial resolution). Additionally, the Cryogenic Near-InfraRed SpectroPolarimeter at the Daniel K. Inouye Solar Telescope (DKIST/Cryo-NIRSP, Fehlmann et al. 2016) will be capable of observing the CO spectrum at a spatial resolution of $\sim 0.''3$ and spectral resolution of $R \equiv \lambda/\Delta\lambda \approx 1.1 \times 10^5$: more than twice the spatial and spectral resolution of the NAC used at the McMath-Pierce. This high-resolution instrument, combined with the excellent seeing characteristics on Haleakalā will provide an unprecedented view of the Sun at 4.7 μm. Both of these instruments are cryogenically cooled, greatly reducing thermal noise in the observed spectra, and will be able to provide high-quality observations of solar CO both on-disk and off-limb.

While both of these instruments are currently installed in standalone configurations (i.e., they cannot share light with other instruments at their telescopes), this work shows that

coordination of CO observations with other diagnostics will be highly fruitful going forward. In particular, coordinated observation of the "cold bubbles" presented here with CYRA or Cryo-NIRSP combined with spectropolarimetric measurements of the chromospheric field using Ca II 8542 Å will allow for a more detailed study of how the solar magnetic field influences their formation, an analysis hindered here by the spectroscopic nature of our IBIS data.

6.3. Phase Spectra and Formation Height

While the CO lines show the most power in the 3–5 mHz frequency band (corresponding to the various 5 minute helioseismic oscillations), their power spectra remain coherent out to at least 6.5 mHz, well past the acoustic cutoff frequency at $\nu = 5$ mHz where traveling acoustic waves can be observed in the photosphere and chromosphere. By examining the phase difference between the power spectrum of a particular CO line and that of a reference line with known formation characteristics, the formation height of that line can be inferred.

Until now, this approach has not been used since it cannot be done with standalone CO observations (needing coordinated observations of a well-characterized reference line). However, since 2011 SDO/HMI has provided synoptic dopplergrams of the solar surface using the photospheric Fe I 6173 Å line at $0\farcs5$ sampling (similar to the spatial resolution of GST/CYRA at 4.7 μm). As shown in Figure 9, these dopplergrams are sufficient to produce coherent phase-difference spectra with strong CO lines like 3-2 R14, even in suboptimal observing conditions.

Therefore, this method can be used to calculate the formation height of CO lines observed with standalone instruments, such as GST/CYRA and DKIST/Cryo-NIRSP. As new, high-quality observations of solar CO are made using these instruments, HMI-CO phase spectra can be used to calculate formation heights at different values of μ, allowing for a more detailed study of the differences between $V-V$ estimates of formation height (as calculated here) and $I-V$ estimates (Penn et al. 2011).

Facilities: McMath-Pierce, Dunn (IBIS), SDO(HMI)

ORCID iDs

Johnathan R. Stauffer ● https://orcid.org/0000-0002-6495-4685
Kevin P. Reardon ● https://orcid.org/0000-0001-8016-0001

References

Anderson, L. S., & Athay, R. G. 1989, ApJ, 346, 1010
Avrett, E. H. 1995, in Infrared Tools for Solar Astrophysics: What's Next?, ed. J. R. Kuhn & M. J. Penn (Singapore: World Scientific), 303
Ayres, T., Penn, M., Plymate, C., & Keller, C. 2008, in 12th European Solar Physics Meeting, ed. H. Peter (Mulhouse: EPS/EAS), 2.74
Ayres, T. R. 2003, in ASP Conference Series, 286, Current Theoretical Models and Future High Resolution Solar Observations: Preparing for ATST, ed. A. A. Pevtsov & H. Uitenbroek (San Francisco, CA: ASP), 431
Ayres, T. R., Plymate, C., & Keller, C. U. 2006, ApJS, 165, 618
Ayres, T. R., & Rabin, D. 1996, ApJ, 460, 1042
Ayres, T. R., & Testerman, L. 1981, ApJ, 245, 1124
Ayres, T. R., & Wiedemann, G. R. 1989, ApJ, 338, 1033
Ayres, T. R. 1998, in New Eyes to See Inside the Sun and Stars, ed. F.-L. Deubner, J. Christensen-Dalsgaard, & D. Kurtz, Vol. 185 (Dordrecht: Springer), 403
Carlsson, M., & Stein, R. F. 1995, ApJL, 440, L29
Carlsson, M., & Stein, R. F. 1997, ApJ, 481, 500
Cauzzi, G., Reardon, K. P., Uitenbroek, H., et al. 2008, A&A, 480, 515
Cavallini, F. 2006, SoPh, 236, 415
Cheung, M. C. M., Schüssler, M., & Moreno-Insertis, F. 2007, A&A, 461, 1163
da Silva Santos, J. M., de la Cruz Rodríguez, J., Leenaarts, J., et al. 2020, A&A, 634, A56
Fehlmann, A., Giebink, C., Kuhn, J. R., et al. 2016, Proc. SPIE, 9908, 99084D
Fleck, B., Couvidat, S., & Straus, T. 2011, SoPh, 271, 27
Fontenla, J. M., Avrett, E. H., & Loeser, R. 1993, ApJ, 406, 319
Freytag, B., Steffen, M., Wedemeyer-Böhm, S., et al. 2010, CO5BOLD: COnservative COde for the COmputation of COmpressible COnvection in a BOx of L Dimensions with l=2,3, Astrophysics Source Code Library, ascl:1011.014
Gudiksen, B. V., Carlsson, M., Hansteen, V. H., et al. 2011, A&A, 531, A154
Hofmann, R., Reardon, K. P., & Milic, I. 2021, AAS Meeting, 238, 205.05
Jaeggli, S. A., Lin, H., Mickey, D. L., et al. 2010, Mem. Soc. Astron. Italiana, 81, 763
Janssen, K., & Cauzzi, G. 2006, A&A, 450, 365
Kopp, G., Lindsey, C., Roellig, T. L., et al. 1992, ApJ, 388, 203
Kurucz, R. L., Furenlid, I., Brault, J., & Testerman, L. 1984, National Solar Observatory Atlas (Sunspot, MX: National Solar Observatory)
Leenaarts, J., Carlsson, M., Hansteen, V., & Gudiksen, B. V. 2011, A&A, 530, A124
Leenaarts, J., Rutten, R. J., Reardon, K., Carlsson, M., & Hansteen, V. 2010, ApJ, 709, 1362
Li, D., Yang, X., Bai, X. Y., et al. 2020, A&A, 642, A231
Livingston, W., & Wallace, L. 1991, An atlas of the solar spectrum in the infrared from 1850 to 9000 cm-1 (1.1 to 5.4 micrometer), NSO Technical Report, National Solar Observatory
Loukitcheva, M., Solanki, S. K., Carlsson, M., & White, S. M. 2015, A&A, 575, A15
Loukitcheva, M. A., White, S. M., & Solanki, S. K. 2019, ApJL, 877, L26
Martínez-Sykora, J., De Pontieu, B., de la Cruz Rodriguez, J., & Chintzoglou, G. 2020, ApJL, 891, L8
Noyes, R. W., & Hall, D. N. B. 1972, BAAS, 4, 389
Penn, M. J., Schad, T., & Cox, E. 2011, ApJ, 734, 47
Pesnell, W. D., Thompson, B. J., & Chamberlin, P. C. 2012, SoPh, 275, 3
Reardon, K. P., & Cavallini, F. 2008, A&A, 481, 897
Scherrer, P. H., Schou, J., Bush, R. I., & Kosovichev, G. 2011, in The Solar Dynamics Observatory, ed. W. D. Pesnell, P. C. Chamberlain, & B. J. Thompson (New York: Springer), 207
Solanki, S. K., Livingston, W., & Ayres, T. 1994, Sci, 263, 64
Stangalini, M., Erdélyi, R., Boocock, C., et al. 2021, NatAs, 5, 691
Stein, R. F., & Nordlund, Å. 1998, ApJ, 499, 914
Uitenbroek, H. 2000, ApJ, 531, 571
Uitenbroek, H., Noyes, R. W., & Rabin, D. 1994, ApJL, 432, L67
Vecchio, A., Cauzzi, G., & Reardon, K. P. 2009, A&A, 494, 269

Vernazza, J. E., Avrett, E. H., & Loeser, R. 1981, ApJS, 45, 635
Wedemeyer-Böhm, S., Kamp, I., Freytag, B., Bruls, J., & Steffen, M. 2006, in
    ASP Conf. Ser. 354, Solar MHD Theory and Observations: A High Spatial
    Resolution Perspective, ed. J. Leibacher, R. F. Stein, & H. Uitenbroek (San
    Francisco, CA: ASP), 301
Wedemeyer-Böhm, S., Ludwig, H. G., Steffen, M., Leenaarts, J., & Freytag, B.
    2007, A&A, 471, 977
Wedemeyer-Böhm, S., & Steffen, M. 2007, A&A, 462, L31
Wootten, A., & Thompson, A. R. 2009, IEEEP, 97, 1463
Yang, X., Cao, W., Gorceix, N., et al. 2020, Proc. SPIE, 11447, 11447AG